



Cite this: *Lab Chip*, 2021, **21**, 3715

## Understanding and improving FDM 3D printing to fabricate high-resolution and optically transparent microfluidic devices†

Reverson Fernandes Quero,<sup>a</sup> Géssica Domingos da Silveira,<sup>a</sup> José Alberto Fracassi da Silva<sup>a,b</sup> and Dosil Pereira de Jesus<sup>a</sup>

The fabrication of microfluidic devices through fused deposition modeling (FDM) 3D printing has faced several challenges, mainly regarding obtaining microchannels with suitable transparency and sizes. Thus, the use of this printing system to fabricate microdevices for analytical and bioanalytical applications is commonly limited when compared to other printing technologies. However, for the first time, this work shows a systematic study to improve the potential of FDM 3D printers for the fabrication of transparent microfluidic devices. Several parameters and printing characteristics were addressed in both theoretical and experimental ways. It was found that the geometry of the printer nozzle plays a significant role in the thermal radiation effect that limits the 3D printing resolution. This drawback was minimized by adapting an airbrush tip (0.2 mm orifice diameter) to a conventional printer nozzle. The influence of the height and width of the extruded layer on the resolution and transparency in 3D-printed microfluidic devices was also addressed. Following the adjustments proposed, microchannels were obtained with an average width of around  $70 \mu\text{m} \pm 11 \mu\text{m}$  and approximately 80% visible light transmission (for  $640 \mu\text{m}$  thickness). Therefore, the reproducibility and resolution of FDM 3D printing could be improved, and this achievement can expand the capability of this printing technology for the development of microfluidic devices, particularly for analytical applications.

Received 11th June 2021,  
Accepted 30th July 2021

DOI: 10.1039/d1lc00518a

rsc.li/loc

### Introduction

Microfluidics has emerged as an extraordinary technology that revolutionized several fields, especially the fabrication of platforms that enable miniaturization of assays and analysis in different analytical and bioanalytical applications.<sup>1</sup> As a result, researchers seek low-cost fabrication techniques and efficient materials to enhance microfluidic capabilities.<sup>2</sup> Moreover, the fabrication of microfluidics and microdevices is always present in borderline research, which becomes evident by recent applications of microdevices on the detection of SARS-CoV-2,<sup>3</sup> a coronavirus responsible for the COVID-19 pandemic. Thus, it increases the need to achieve the full potential of fabrication techniques that provide less expensive devices using novel and low-cost materials.

In the past decades, glass and silicon materials were usually applied, offering high precision<sup>4</sup> but requiring complex, time-consuming, and costly fabrication methods. As an attractive alternative, polymers started to be used, particularly poly(dimethylsiloxane) (PDMS), poly(methylmethacrylate) (PMMA), high-density polyethylene (HDPE), low-density polyethylene (LDPE), polyamide 6, and SU-8.<sup>2,5</sup> The most popular method to fabricate microfluidic devices with such materials, particularly PDMS, was the soft-lithography technique. This microfabrication technique is based on replicating molds using elastomeric materials following several fabrication steps.<sup>6</sup> PDMS micro-molding was widely used up to the last ten years, but requirements of multi-step processing, difficulties to quickly change the design of the devices, and the demand for commercial upscaling prompted researchers to develop alternative techniques for the fabrication of microfluidic devices.<sup>7,8</sup>

New possibilities became feasible with the advent of additive manufacturing technology or three-dimensional (3D) printing, as it is usually called.<sup>8,9</sup> 3D printing has emerged as a layer-by-layer technology to fabricate 3D objects and platforms directly from computer-aided design (CAD) drawings.<sup>10</sup> Firstly, a CAD model is digitally divided into a stack of horizontal cross-sections (slicing processes). The

<sup>a</sup> Institute of Chemistry, State University of Campinas, Campinas, SP, 13083-861, Brazil. E-mail: dosil@unicamp.br

<sup>b</sup> Instituto Nacional de Ciéncia e Tecnologia em Bioanalítico (INCTBio), Campinas, SP, Brazil

† Electronic supplementary information (ESI) available: Assembly and configuration of the FDM-based 3D printer; printing parameters; thermal and vibrational tests; pressure tests; computational simulations; statistical analysis; tutorial videos. See DOI: 10.1039/d1lc00518a

software then transforms the slices into a coordinate model to be sent to the printer, and finally the object is printed layer-by-layer, generating a 3D-printed model similar to the digital version.

Microfluidic device fabrication has been benefited from the advantages of 3D printing. In contrast with soft-lithography, 3D printing allows higher design flexibility, rapid prototyping, complex geometries, interconnects integration, one-step sealing, and compatibility with the commercialization scale.<sup>11</sup> Fused deposition modeling (FDM), stereolithography (SLA), inkjet/polyjet (i3DP), two-photon lithography, selective laser sintering (SLS), and layered hydrospinning are examples of 3D printing approaches commonly used.<sup>12</sup> Many reviews dedicated to 3D-printed microfluidic fabrication have been reported in the literature, mainly regarding the challenges and applications<sup>1,12–15</sup> from biological<sup>14,16,17</sup> and chemical analysis<sup>18</sup> to the synthesis of nanomaterials.<sup>19–21</sup>

Macdonald and co-workers compared the performance of three dominating printing technologies, FDM, i3DP, and digital light processing stereolithography (DLP-SLA), on microfluidics fabrication. The results showed that FDM was suitable for microfabrication with minimum features of  $321\text{ }\mu\text{m} \pm 5\text{ }\mu\text{m}$ , while i3DP and DLP-SLA fabricated channels with a minimum width of  $205\text{ }\mu\text{m} \pm 13\text{ }\mu\text{m}$  and  $154\text{ }\mu\text{m} \pm 10\text{ }\mu\text{m}$ , respectively.<sup>22</sup> The authors suggested that DLP would be suited for microfluidic applications where precise control of features and fluidics is critical, while i3DP offered the highest price per device. Even with the highest channel resolutions achieved by DLP-SLA, this technique often requires cytotoxic reagents and presents limited multi-material capabilities.

In this context, FDM printers are considered an attractive technology, especially because of the low cost of acquisition, ease of operation, and compatibility with a wide range of thermoplastic polymers, such as polyethylene terephthalate glycol (PETG), polylactic acid (PLA), polycarbonate (PC), cyclic olefin copolymer (COC), thermoplastic polyurethane (TPU), polymethylmethacrylate (PMMA), polypropylene (PP), and acrylonitrile butadiene styrene (ABS).<sup>13,23</sup> Additionally, using printers equipped with multiple printer nozzles, multi-material printing is feasible. This FDM feature is advantageous because materials with different compositions and properties can integrate distinct functionalities into the fabricated device, using a unique printing process.<sup>24</sup> However, FDM-based 3D-printed microdevices show crucial challenges to overcome, including low resolution, low optical transparency, high surface roughness, and difficulties in creating small internal fluidic features.<sup>11,13,23</sup> Bhattacharjee *et al.* (2016) highlighted three main reasons for that: firstly, the filaments laid down by the extrusion process cannot be arbitrarily joined at channel intersections. Consequently, the lack of structural integrity between the layers results in weak seals, and sometimes devices cannot hold over 20 bar pressure without leakages; and finally, the size of the filaments extruded are larger than typical channels used in microfluidics.<sup>7</sup>

Some authors have tried to overcome such problems, especially through adjusting the slicing parameter in the printer software, producing 3D-printed microfluidic devices with channel dimensions under  $100\text{ }\mu\text{m}$  using TPU polymer.<sup>25</sup> Previously, Romanov *et al.* (2018) showed that the resolution of FDM-based 3D printers commercially available was still  $250\text{--}300\text{ }\mu\text{m}$  using PLA,<sup>26</sup> close to that observed by Bressan *et al.* (2020) using the same polymeric material.<sup>21</sup> However, it is necessary more than software optimization to achieve the full printing potential of FDM printers, especially because advertised specifications of a printer rarely match the minimum printable feature size. Thus, researchers often find discrepancies in the printer resolution and the creation of tiny features required for microfluidic fabrication.

Therefore, in this work we systematically studied the parameters related to printing resolution, such as nozzle features, frame and printing bed, layer height (thickness), extrusion width (raster), and others. We propose physical adaptations to achieve the full potential on FDM printers to obtain microfluidic and transparent devices that can be used for analytical and bioanalytical applications. To the best of our knowledge, no work has been published demonstrating such detailed changes in the components of the printer and their impact on the printing process.

## Theoretical background

### Nozzle influence on the printing process

Although FDM-based 3D printing has brought many advances in the printing processes of several devices, some challenges remain, particularly regarding optimizations on the components of the printers to obtain better quality and resolution in the printed devices. In this context, the extrusion nozzle plays a fundamental role concerning the resolution because it is the component of the printing system that is in contact with the filament before it is extruded into the printing bed. Thus, the characteristics of the nozzle can provide a better quality of the printed parts, particularly improving the resolution. Moreover, several authors have systematically discussed its importance related to the diameter,<sup>20,27</sup> pressure,<sup>28</sup> printing speed,<sup>29</sup> and material flow.<sup>30</sup>

The nozzle follows the pattern sent by the software to the machine through G-codes, and the object is built layer-by-layer. Thus, the diameter and length of the nozzle become important characteristics since each melted layer solidifies and sticks to the previous layer, repeating the process until the product is finished.<sup>31</sup> Other characteristics include the composition and external shape of the nozzle.

The composition of the nozzles can vary among copper and steel alloys, titanium, and aluminum oxide. The materials are associated with thermal properties, such as conductivity and expansion coefficients, which are directly related to the maximum temperature reached during the printing.<sup>32</sup> Moreover, the composition of the nozzle can also

affect the thermal radiation transference between the metallic and printed surfaces.

The length of the nozzle may be related to the amount of filament that it heats up during extrusion. Longer nozzles provide more surface area available for transferring heat to the filament, making the extrusion process more efficient and rapid. Moreover, the inappropriate temperature in the nozzle affects the adhesion of the layers in the printing process.<sup>31</sup>

Some nozzle models commercially available are depicted in Fig. 1. It is possible to observe that among these nozzles, the length of the noses (indicated in Fig. 1 as distance A) and the total length of the nozzle (indicated as distance A + B + C) vary. Usually, nozzles with a long total length can provide better filament heating because their heating area increases.

Furthermore, different shapes and geometries of the nozzle head are available with wider or pointed noses, as shown in Fig. 1-III. Volcano and ED3-V6 (Fig. 1-III) are examples of flat noses, while the pointed ones are MK10 and MK7/8. Compared to those with flat noses, the last ones present an advantage regarding reducing undesired heat transfer to the material already deposited. Ensuring that the material extruded cools quickly after the extrusion is an important criterion for the quality and resolution of FDM 3D printing. In this way, an equation to evaluate the geometrical influence (GI) of the nozzle features on the FDM 3D-printing process can be deduced based on the previous works of Liang<sup>30</sup> and Brooks,<sup>33</sup> and it can be defined as:

$$\text{G.I.} = \frac{b_N}{(\theta_s)} + \left( \frac{\ell \cdot r}{2} \right) \quad (1)$$

where  $\theta_s$  is the angle (in radians) of the nozzle tip in relation to the printing surface,  $b_N$  indicates the length of the nose (in mm),  $\ell$  is the length of the arc (in mm), and  $r$  is the height of the base to half the height of the nozzle (in mm) (shown as distance A in Fig. 1-I). According to eqn (1), a larger nose (flat head) implies greater  $b_N$  and  $\ell$ , so the angle

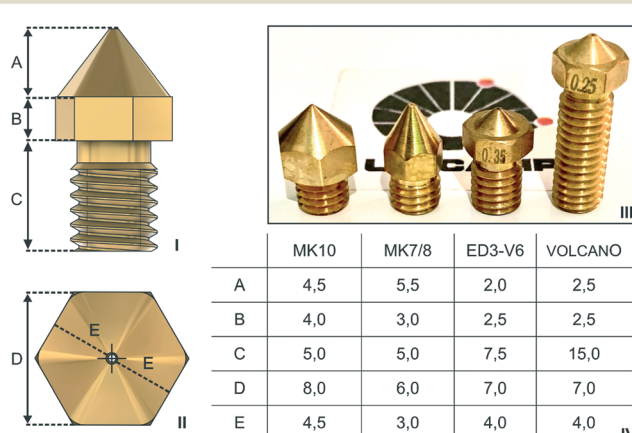


**Fig. 1** Different nozzle models commercially available. I) Side profile of the nozzle; II) top view of the nozzle; III) four models available; IV) table with dimensions of each part (A–E) presented in millimeters.

of the nozzle tip in relation to the printing surface is diminished, and the GI values are increased together with an undesired thermal transfer effect.<sup>34</sup>

The orifice diameter of the nozzle generally ranges from 0.1 to 1 mm, and 0.4 mm is a standard nominal value for the nozzles used in commercial FDM printers. Some important printing parameters related to resolution depend on the nozzle orifice diameter, such as layer thickness, raster width, air gap, and printing speed.<sup>35,36</sup> Commonly, larger orifice diameters will extrude more material, and consequently, thicker and wider layers are reached with a speed gain but with loss of resolution. On the opposite, smaller orifice diameters (less than 0.4 mm) can produce detailed prints with barely noticeable layer marks. However, a lower flow rate of the extruded material through the nozzle means a slower printing speed. It is also important to emphasize that a larger orifice diameter does not mean a larger nose, being that one related to the internal diameter of the tip.

Sukindar *et al.* (2016) compared the printing time obtained using nozzles with different orifice diameters ranging from 0.2 to 0.4 mm. According to the achieved results, the nominal diameter of 0.2 mm had the highest printing time. Moreover, the authors also showed that the diameters of 0.2 and 0.25 mm provided the highest pressure drop, which significantly affects the consistency and quality of the road widths.<sup>27</sup>

### Printing parameters and interaction between layers

The most important printing parameters related to the resolution in microdevices are layer thickness, raster width, air gap, extrusion flow rate, and printing speed. These parameters are directly associated with the interaction between the printed layers and some components of the printers, such as the nozzle. Thus, several authors have been dedicating efforts to evaluate the influence of these critical parameters on the mechanical properties and the dimensional accuracy of the printed device.<sup>20,21,37–39</sup>

The extrusion flow rate (extrusion multiplier) is related to the amount of filament that comes out of the nozzle. This parameter is essential for the accuracy of the printing process because an unsuitable (insufficient or excessive) extrusion flow rate can lead to printed parts with low resolution and optically opaque appearance.<sup>40</sup>

The printing speed usually is defined as the amount of filament deposited (extruded) per time unit. The decrease of the printing speed can improve the resolution, but if this speed is extremely low, the long time that the extruding nozzle remains close to the printed surface favors the undesirable thermal radiation effect, as will be discussed ahead. Although high printing speeds allow short printing times, the quality of the finishing surface (imperfections and failures) and the adhesion of the printed layers can be reduced. Thus, the printing speed should be set appropriately according to the extrusion flow rate to achieve high-quality printing.<sup>41</sup>

As aforementioned, the thickness of the extruded layer depends on the diameter of the extruder nozzle, and it has a significant influence on the surface roughness and printing time. The distance of the gap between the nozzle and the printing bed determines the height of each layer. Generally, this gap is less than the orifice diameter of the nozzle, and it has been considered at around 0.06 to 0.6 mm.<sup>31</sup>

Furthermore, an important factor in 3D-printing microdevices is the precise alignment and strong bond between the deposited layers, especially because FDM-based printing can create voids or air gaps if the layers are not uniformly bound. These air gaps are the space between the adjacent raster and the vertical layers. A good way to decrease these spaces is to increase the raster width, which is defined as the width of the adjacent deposition layers.<sup>35</sup> To tentatively minimize the empty spaces created between the junction of the layers (voids), Wang *et al.* (2016)<sup>42</sup> proposed adding thermally-expandable microspheres to the materials used for the printing process.

Fig. 2 illustrates both the vertical deposition of the layers (layer height) and the horizontal deposition of the raster (raster width) and the interaction between them (sintering).

The sintering process occurs at temperatures above the glass transition of the printing material when it becomes viscous or rubbery. Some authors report that most neck growth occurs during the first phase of the process and at temperatures above a critical sintering temperature (*e.g.*, about 180 °C for PLA and 200 °C for ABS).<sup>37,43</sup> The spreading rate and the final shape of the extruded filament are dependent on the viscosity of the material and the relative surface energies between the deposited layers. After the material is extruded and sintered, it starts to cool, and the viscosity increases until a solid state is reached. The rounded and oblong shapes of the deposited raster lead to small voids in the printed objects (Fig. 2-A), and it can also affect the transparency of the printed objects. In this context, we can simplify Frenkel's model for sintering presented by Pokluda and co-workers<sup>44</sup> by considering the interaction of two deposited layers as being two spheres of the same height ( $H$ ) and length ( $W$ ), at time  $t$ , and both centers moved to interpolate and create an overlap with a distance of intersection  $\theta$  and the radius of the neck  $\alpha$ , as depicted in Fig. 2-C.

Moreover, Costa *et al.*<sup>45,46</sup> studied the contribution of several phenomena of heat transfer in the adhesion of the layers, including the thermal radiation of the environment, the thermal conduction between the adjacent rasters, and the convection of surrounding air, besides the magnitude of the mechanical deformations between the layers. Based on this study, Garzon-Hernandez *et al.*<sup>47</sup> proposed algorithms correlating the heat transfer processes and the interaction between the layers of the deposited materials. Eqn (2) demonstrates the effect of the temperature on the interactive process between the filaments, as depicted in Fig. 2.

$$T_r(x, t) - \frac{\sum_{j=1}^m a_{rj} h_j \lambda_j T_{rj}(t)}{K_1 + K_2} \left[ 1 - e^{\beta(t-t_r(x))} \right] = T_{\text{extr}} e^{\beta(t-t_r(x))} \\ + \frac{K_1 T_E}{K_1 + K_2} \left[ 1 - e^{\beta(t-t_r(x))} \right] + \frac{a_r \text{supp} \lambda_1 h_{\text{supp}} T_{\text{supp}}}{K_1 + K_2} \left[ 1 - e^{\beta(t-t_r(x))} \right] \quad (2)$$

where  $T_r(x, t)$  is the temperature at location  $x$  and in time  $t$  of a given filament  $r$  (°C);  $a_r$  is a variable which receives the value 1 if the filament segment  $r$  is in contact with another segment, and 0 if there is no contact;  $\lambda$  is the fraction of the filament area in physical contact with another filament (used  $n \leq 4$  to simplify) of perimeter  $P$ ;  $h$  is the contact heat transfer coefficient (W m<sup>-2</sup> °C<sup>-1</sup>);  $T_{\text{extr}}$  is the extrusion temperature;  $T_{\text{supp}}$  is the temperature of the support;  $h_{\text{supp}}$  is the heat transfer coefficient (W m<sup>-2</sup> °C<sup>-1</sup>) between the filament and the support segment. A more detailed description of eqn (2) and its derivation can be found in the work of Costa and co-workers.<sup>45</sup>

It is important to emphasize that  $K_1$  and  $K_2$  define the heat transfer by convection with the environment and the heat transfer by conduction between the adjacent filaments (or support structure) per unit of temperature, respectively. Thus, the temperature can influence both the interaction between the filaments (or between the filament and the support) and the heat transfer with the external environment.

Other authors have assumed analytical and numerical models for simulating the heat transfer between the layer in the extrusion process and the layers already printed, especially regarding the neck growth (bond formation with time) to achieve the predicted size of the layers.<sup>48</sup> The neck

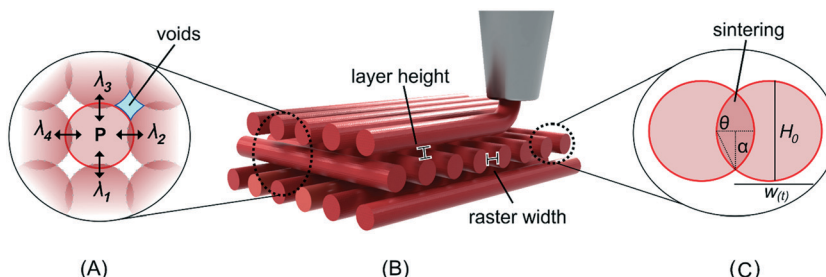


Fig. 2 A) Scheme of interaction between layers, where  $\lambda$  is the fraction of the filament area in physical contact with another filament. B) Representation of the deposition of the material both in the width of the raster and in the height of the layers. C) Sintering of the adjacent raster based on Frenkel's model,  $H_0$  is the layer height,  $W(t)$  is the length of the raster,  $\theta$  is the intersection distance, and  $\alpha$  is the radius of the neck.

influences the mechanical resistance as well as the dimensional accuracy of the manufactured part. The non-uniform thermal gradients and the viscoelastic material behavior of the polymer need to be considered in the development of prediction models, and this issue is addressed in work by Penumakala *et al.* (2020).<sup>49</sup>

Besides the work reported by Costa *et al.* (2015),<sup>45</sup> Wolszczak *et al.* (2018) have shown that the radiation effect of the heated printer components, particularly the heat emitted by the head of the nozzle, can increase the temperature of the previously deposited layer.<sup>50</sup> According to the authors, the design of the used head holder can cause more intensive and non-uniform heating.

Finally, effective control of both the extrusion temperature and thermal radiation of the printer components plays a crucial role in determining the final resolution and the quality of the printed components, especially in the fabrication of microfluidic devices.<sup>51</sup>

## Experimental

### FDM-based 3D printer

An FDM-based 3D printer based on an open-source project was assembled by using a modular and enclosed structure. The printer was equipped with a double extrusion system controlled by a controller board with a 32-bit chip and open-source firmware. The components used and all file configurations are available in Table S1 in the ESI† section (Section S1), as well as the assembling diagram, which is depicted in Fig. S1 and S2.† An adapted and optimized nozzle with a diameter of 0.2 mm and 8 mm height was used, as described in the ESI† section, and it is depicted in Fig. S3.† The procedure for adaptation of the nozzle is shown in Video S1.†

### Design and fabrication

The design of the microfluidic devices was accomplished using Autodesk Inventor (professional version 2020) software (Autodesk, San Rafael, California) and exported in STL file. The slicing and printing settings were controlled with Simplify3D (version 4.1) software (Blue Ash, USA) that generated the G-code commands for the 3D-printer. The filaments for the FDM-based 3D-printer made of acrylonitrile–butadiene–styrene (ABS), modified polyethylene–terephthalate–glycol (PETG), poly(lactic acid) (PLA), and thermoplastic polyurethane (TPU) were supplied by 3DX Filamentos (São Caetano, São Paulo, Brazil). Among these filaments, PETG was chosen because it demonstrated the best performance based on optical transparency, mechanical resistance, and morphological resistance to solvents for printing the microfluidic devices.

Several devices were designed and tested, and their drawings and respective used files are available for download (Table S2†), while the printing parameters are shown in Table S3.† The device used for experimental planning and robustness tests had 15 mm × 43 mm dimensions and 0.7

mm thickness. The designed microfluidic devices comprised channels of 140 µm × 160 µm with 35 mm in length and 4 reservoirs of 3 mm in diameter. However, real channel dimensions may change according to the printing parameters used and the thermal deformation rate of the filaments.

The printing parameters of the main devices were: layer height 0.08 mm; extrusion width 0.12 mm; multiplier extrusion 104%; extruder temperature 235 °C; bed temperature 100 °C. The common printing parameters for all devices were: infill 100%; print speed 10 mm s<sup>-1</sup>; internal and external infill angle +45° and -45°. Other printing parameters can be found in the ESI† (Section S2). The modeling, slicing, and printing files are also available for download as open files (Table S2,† Section S2).

### Characterization of the microdevices

The fabrication of the microdevices was evaluated according to microchannel dimensions, transparency, pressure resistance, thermal simulations, and vibrational tests, as described in the following sections.

**Thermal and vibrational tests.** The thermal images were obtained with a Flir camera, model C5 of 19 200 pixels (Flir Systems, Arlington, USA), using lava and iron thermal filters with scale IR from 40 to 300 °C. Vibrational tests were carried out by assembling an open-source system using a common piezoelectric vibration sensor module with an Arduino UNO controller, as depicted in Fig. S4 and S5.† Moreover, two FDM-based 3D printers with an open cabinet Cartesian and another one with a cabinet CoreXY enclosed were assembled and used to perform thermal and vibrational tests.

**Simulations and statistical analysis.** Thermal simulations were performed using computational fluid dynamics software Autodesk CFD, with the Thermal Simulations package (version 2020). All components of the extrusion system, such as the heating block, nozzle, heating cartridge, thermistor, throat tube, and cooler fan, were designed with real dimensions. Additionally, the material composition of the components was also respected in the simulations; for instance, aluminum was used for the heating block, copper for the nozzle, and stainless steel for the tip, as summarized in Fig. S6.† Other parameters used for the modeling are described in the ESI† (Section S3).

Statistica software (TIBCO™ Software Inc., Palo Alto, USA) was used to carry out the experimental planning. The experimental design chosen was Box–Behnken using three variables: layer height, extrusion width, and multiplier extrusion with three levels each, as depicted in Table S4.†

**Transparency, channel size measurements, and pressure tests.** The image and microchannel size analyses were conducted using an Axio Observed A1 inverted optical microscope from Zeiss (Oberkochen, Germany), equipped with an HBO 100 light source for fluorescence with a filter set 38 and HAL 100 light source for optical analysis. The images were acquired with an Axio Cam MRc, using 5× to 40× objectives.

A transmission meter, model LS162 from Linshang (Shenzhen, China), was used to perform visible light transmission tests in the 3D printed devices with a thickness of 640 µm (total of 8 printed layers). Measurements of visible light transmission (from 380 to 760 nm) with 0.1% resolution and  $\pm 2\%$  accuracy were performed on 17 devices. The measurement procedure is shown in Video S2† (Section S4†).

The pressure tests were carried out with a digital manometer model 550 from Testo (West Chester, USA) using a valve manifold coupled in the outlet reservoir (microdevice) and a syringe pump, model Pump 11 Elite (Harvard Apparatus), in the inlet reservoir, as depicted in Fig. S7.†

## Results and discussion

### Influence of the nozzle features and thermal radiation effect

Several parameters were evaluated to achieve suitable channel widths (for microfluidics) in FDM-based 3D-printed devices. First of all, seven commercially available extruder nozzles with different orifice diameters were used to print microchannels with the minimum feasible size. Fig. 3 depicts the results obtained for the nozzles with nominal diameters ranging from 100 to 400 µm (Fig. 3-A).

Microscopy images of the nozzle orifices in Fig. 3-B showed a significant difference between the nominal and real values of the diameter, with the most discrepancy being observed for nozzle II with 150 µm and 118.14 µm for the nominal and measured values, respectively. Thus, based on the real diameter values, a correction may be performed on the software to achieve microchannels with more reproducible sizes.

Although smaller nozzles can extrude larger rasters, they present greater flow restrictions when compared to larger nozzles. Therefore, the printing speed must be reduced to reach better results, even if the printing time is significantly increased. A printing speed of 10 mm s<sup>-1</sup> was selected using

an infill of 104%, and the results are addressed in the next section.

According to the results depicted in Fig. 3-C, it is possible to observe that microfluidic channels were obtained with widths ranging from 394 to 132 µm with standard deviations varying from 21 to 31 µm. No substantial gain in the resolution was achieved in the microchannel using nozzles with orifice smaller than 200 µm. This result is related to the thermal radiation derived from the nozzle, which avoids using extrusions with low raster width. This limitation corroborates with the expected effect of the nozzle body diameter on the 3D printing resolution. Thus, the thermal radiation effects associated with the nozzle geometry, especially the distances A and D indicated in Fig. 1-I and -II, were considered.

The thermal radiation effect became clear by the computational simulation results shown in Fig. 4. The results evidenced that the deposited raster suffers a reheating by the thermal radiation from the nozzle and its neighborhood (Fig. 4-A) that can reach more than 200 °C. The consequence of these high temperatures in the raster adjacency is the increase of defects and the loss of resolution. Moreover, in Fig. 4-B it is also possible to observe that a specific temperature on the standard nozzle to reach the extrusion of the material also promotes heating around the nozzle support structure.

An adaptation of the nozzle was proposed and evaluated to overcome the thermal radiation effect using a commercial brass nozzle coupled to an airbrush tip of stainless steel with 0.2 mm orifice diameter, as detailed in the ESI† (Section S1). Thus, an adapted nozzle with a final height of 8 mm and 0.2 mm orifice diameter was achieved (Fig. 5), and a video showing the adaptation steps can be accessed in the ESI† (Section S4).

Fig. 6-A compares the thermal simulations for both nozzles (standard and adapted) and shows the final printed devices obtained by using them. The values used for heat

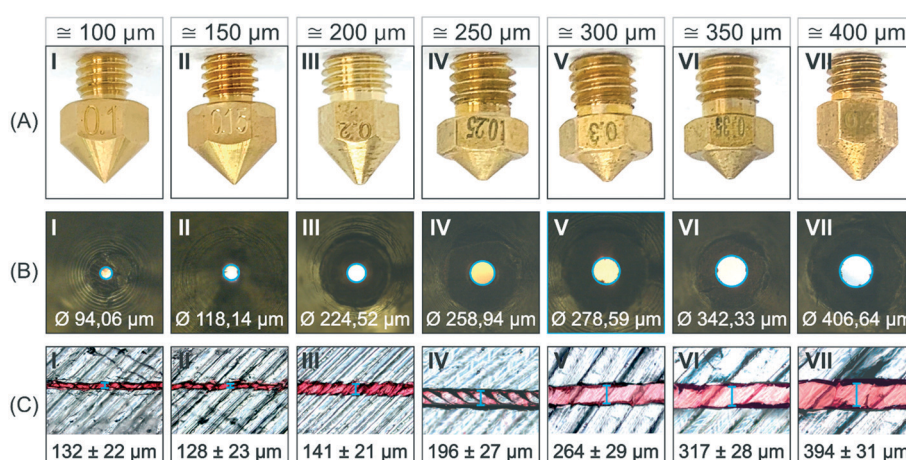


**Fig. 3** (A) Commercial nozzles with different nominal diameters: I. 100 µm, II. 150 µm, III. 200 µm, IV. 250 µm, V. 300 µm, VI. 350 µm, VII. 400 µm. (B) Microscopy images of the nozzle orifices and the measured diameter values. (C) Images of the microchannels (with the minimum width obtained using each nozzle, and the average of the widths measured ( $N = 25$ ) for 5 different devices).

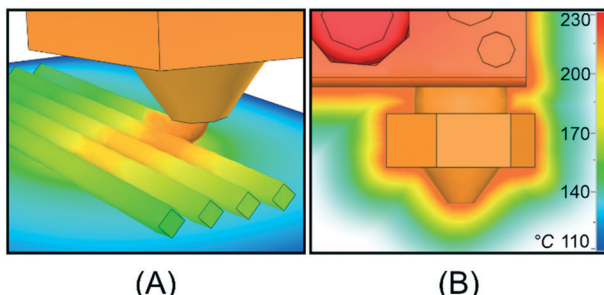


**Fig. 4** A) Simulation of the raster deposition and effect of the temperature on adjacent deposited layers. B) Simulation of the thermal radiation and temperatures from the extruder nozzle and its support structure.

loads and thermal limit conditions were selected according to the real values to have a faithful model. Thus, a thermal load of 230 °C was selected for the heating cartridge, and the contact detection tolerance was fixed at 0.10 mm for all parts. The thermal radiation between the hot end and the printed device has an emissivity value of 0.95. The simulation results included both the temperature of contact and heat flow. Then, the same extrusion temperature was applied for both nozzles, and comparatively, the adapted nozzle showed a decrease in heat dissipation.

For the adapted nozzle, a decrease in the heated area around the nozzle was found, and consequently, a more negligible radiation effect from the head of the nozzle to the printing surface (Fig. 6-A) was observed. More detailed results for computational thermal simulation are provided in Fig. S8.<sup>†</sup>

Using a thermal camera to perform thermographic analysis, it was possible to find (Fig. 6-B) that the temperature of contact for the standard nozzle is locally higher than that observed for the adapted nozzle, with values of 173 and 138 °C, respectively. Moreover, the XY movement of the extrusion system through the printing surface and a greater heat flow lead to a reheating of the previously deposited layers resulting in a non-uniform bond between them. This reheating was observed in the results depicted in Fig. 6-D, where the XY movement of the standard nozzle led

to deformation in the printed parts. This non-suitable printing can be particularly associated with the proximity needed by the nozzle for raster deposition, keeping the region warm for a longer time. On the opposite, the adapted nozzle allowed a suitable distance between the tip and the printing surface, preventing an excessive heat flow and leading to a more uniform printed structure, as shown in Fig. 6-D.

Other images were collected to confirm the simulations performed, and the thermographic analysis of the different parts of the system is shown in Fig. S9.<sup>†</sup> The results observed corroborate the use of the adapted nozzle to achieve better resolution, mainly because of the decrease in the thermal radiation effect, resulting in 35 °C lower than that observed for the standard nozzle. Thus, the adapted nozzle can improve the XY resolution by diminishing the space between the raster deposition, and consequently it improves the resolution of the channel width in microfluidic devices.

The results achieved can also be explained in terms of a theoretical framework, particularly following the eqn (1) suggested in the theoretical background for GI of the nozzle. Fig. 7 compares the features of the standard and adapted nozzles, and it can be noted that the angle of the nozzle tip ( $\theta_s$ ) related to the printing surface is greater for the adapted nozzle (Fig. 7-B). Moreover, the length of the arc ( $\ell$ ) and the length of the nose ( $b_N$ ) are lower than those for the standard nozzle. Consequently, the values of GI are decreased for the adapted nozzle, leading to the reduction of the undesired thermal transfer effect. Thus, the results were in close agreement with the theory, in which more pointed nozzles promote lower GI values, and they produce a better precision in the deposition of the extruded material.<sup>34</sup>

### Influence of the layer height and extrusion width

A common way to overcome the deformation in the 3D printed parts is to optimize the layer height in the software parameters. However, it is not an interesting solution for microfluidic devices, particularly because higher layer height values can increase the formation of air gaps and voids because of the weak bonding of the layers. Consequently, leakage and problems with the sealing of 3D-printed FDM-based devices are commonly observed. This problem can be better visualized in Fig. 8, where the consequences of too low or high values of layer height in the printed devices are illustrated.

As shown in Fig. 8A and C, layer height  $\geq 150 \mu\text{m}$  or  $\leq 50 \mu\text{m}$  can promote a deformation in the printed devices, especially because of the weak bonding between the layers (high layer height) and excessive fusion (low layer height). The ideal layer height is observed in Fig. 8B, where the distance between the tip and the printing surface is suitable, ranging from 80 to 120  $\mu\text{m}$ , for obtaining 3D-printed devices with few deformations. The defects observed are more pronounced when a flat nose is used even though ideal parameters are applied, mostly due to the undesired reheating effect. Fig. S10<sup>†</sup> compares printed devices obtained

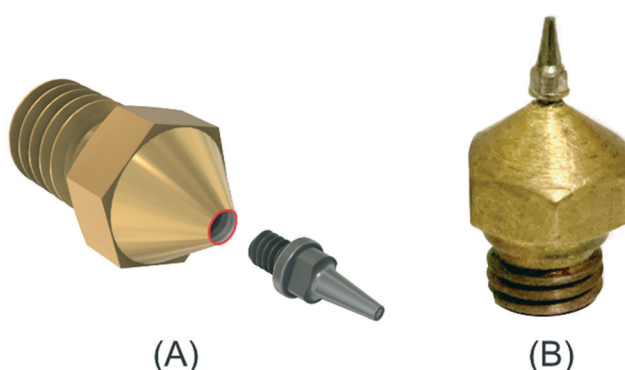


**Fig. 5** A) Illustration showing the adaptation of the nozzle and the B) actual image of the adapted nozzle.

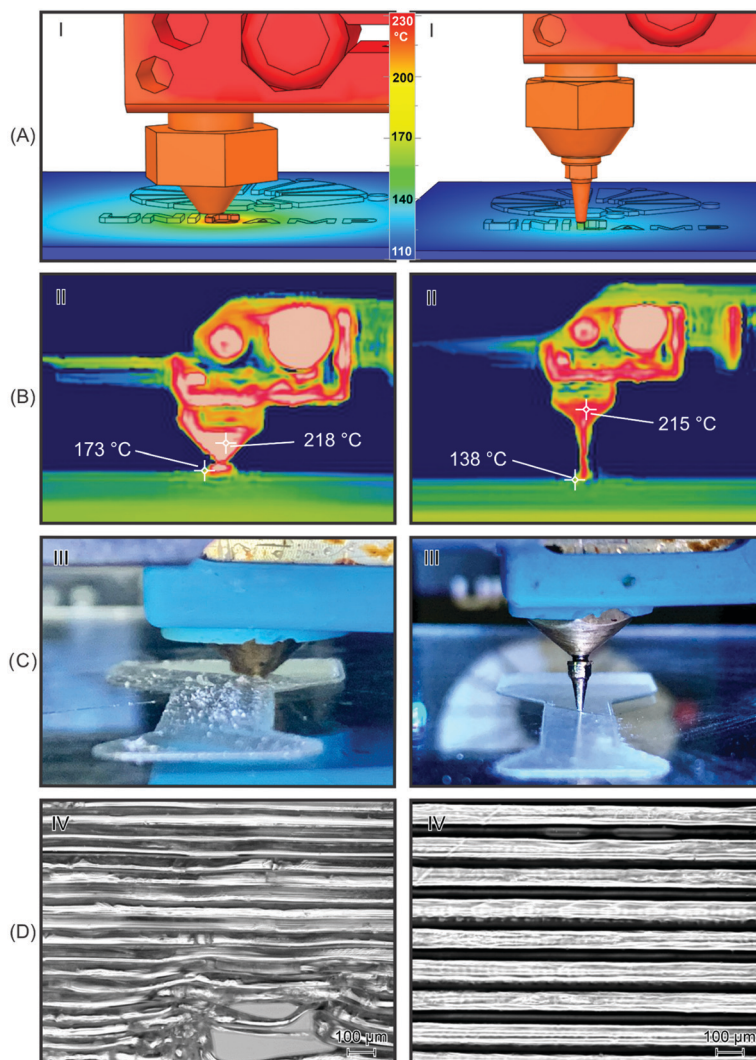


**Fig. 6** A) Computational thermal simulation for the standard and adapted nozzle; B) thermographic analysis of the extruder head: temperatures of the heating cartridge and temperature of contact; C) XY movement of the extrusion system; D) close up images of the surface of the final printed parts using both nozzles.

using both nozzles when an ideal height layer is applied. Thus, the use of pointed nozzles allowed a greater sintering between the rasters, and consequently, a smaller height layer

and raster width can be used. As a consequence, a superextrusion can be reached (extrusion multiplier or extrusion flow rate >100%) to obtain a greater filling of the empty spaces between the layers (voids and air gaps) without promoting deformation.

Furthermore, the differences between the real and nominal orifice diameters of the nozzle require a correction in the height layer and raster (extrusion) width to achieve a microchannel with more reproducible sizes. For that, it was found that the real value may be indicated in the “nozzle diameter” option of the slicing software as suggested by the following ratio:

$$\frac{\text{Raster width}}{\text{Layer height}} \geq 1.2 \quad (3)$$

This ratio between the raster width and the layer height may be equal or greater than 1.2 for a better infill

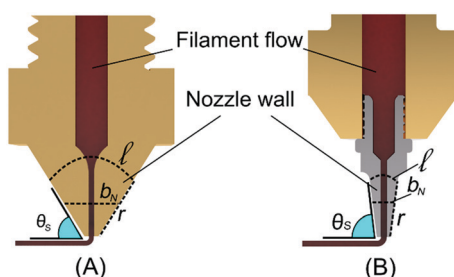


**Fig. 7** Geometric features of the (A) standard and (B) adapted nozzle.  $\theta_s$  is the angle of the nozzle tip in relation to the printing surface (in radians),  $b_N$  indicates the length of the nose (in mm),  $\ell$  is the length of the arc (in mm), and  $r$  is the height of the base at half the height of the nozzle (in mm).

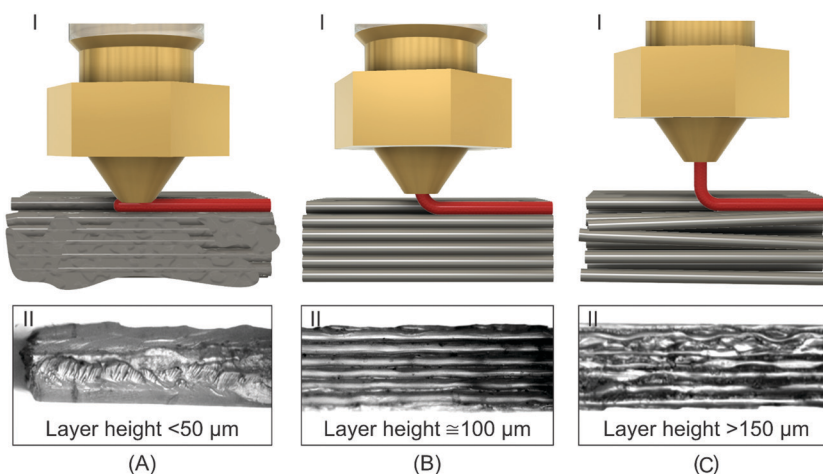


**Fig. 8** Consequences of using too low layer height (A), an ideal layer height (B), and too high layer height values (C); (I) hypothetical nozzle illustrating the layer height, and (II) the object printed under such conditions.

and adhesion among the layers. The maximum layer height must be between 50 and 75% of the nozzle

diameter, while the raster width is usually calculated by the software.

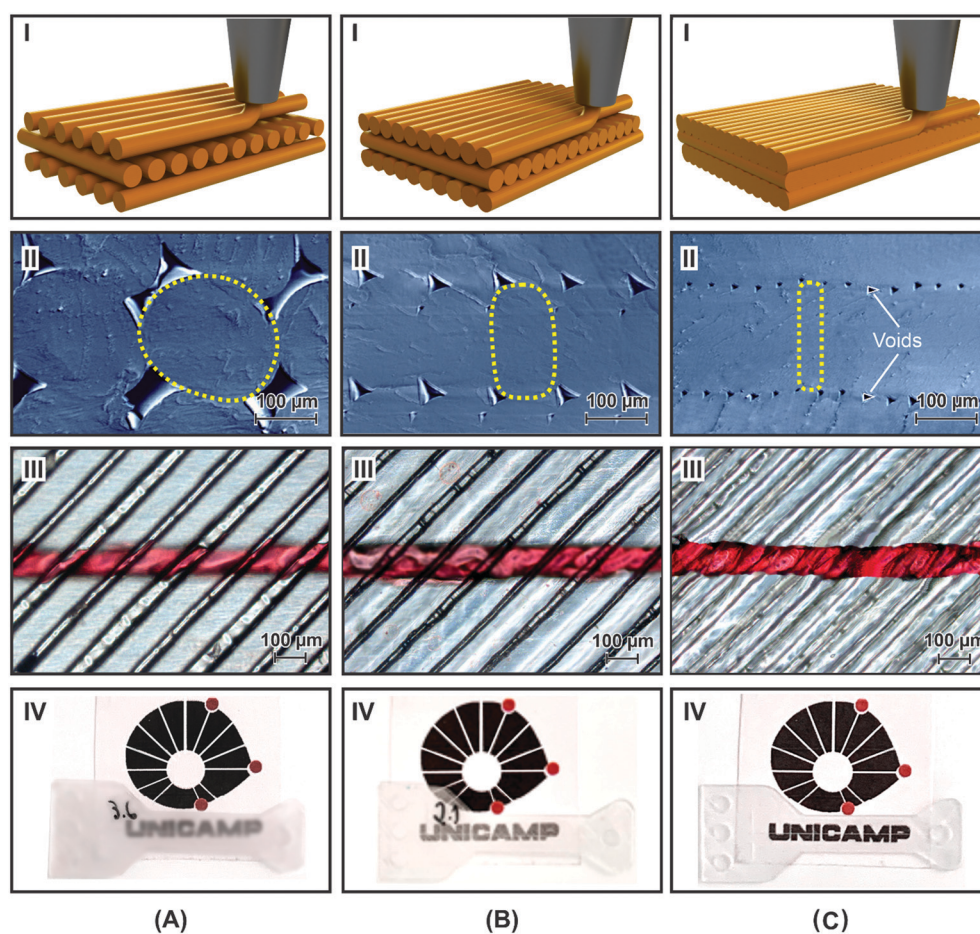


**Fig. 9** Printing tests performed using (A) layer height of 0.12 mm, width of 0.22 mm and extrusion multiplier of 0.96 (96%), (B) layer height of 0.10 mm, width of 0.20 mm and extrusion multiplier of 1 (100%), and (C) layer height of 0.08 mm, width of 0.18 mm and extrusion multiplier of 1.04 (104%). Figures show (I) a 3D illustration scheme of the printing process for each condition, (II) SEM images of the raster shapes, (III) microscopy images of the top layer above the channel in the printed device, and (IV) real images of the transparent printed devices.

The choice of the parameters in the 3D-printing process can be a difficult task, and although there are basic rules, particularities related to the project, the printer components or the design may require changes of the default parameters. Thus, it is advisable to configure the raster width manually, maintaining the extrusion layer greater than 80% of the nozzle diameter.

### Transparency of microfluidic devices: relation between layer overlap and software parameters

Besides the quality of printed devices, layer height, raster width, and extrusion multiplier (extrusion flow rate) are important parameters to define transparency in a microfluidic device. The transparency in FDM-based 3D-printed microfluidic devices opens several possibilities for applications. However, obtaining transparent devices with this technology can be challenging regarding choosing the parameters used and the printing material. Moreover, transparency is related to the tendency of the material to diffract light that can be a result of many factors, but especially the homogeneity in FDM-based 3D-printing. As aforesaid, the homogeneity of the printing is related to the low number of voids and air gaps between horizontal deposition and overlap of vertical layers.

Although some polymeric materials are inherently transparent, such as PETG, this is not a condition to obtain transparent devices once the layer height and raster width can significantly influence the final transparency. In this context, preliminary printing tests were performed using PETG with different combinations of the parameters to evaluate the influence on the transparency. The first results shown in Fig. 9 were obtained using a layer height and width of (A) 0.12 and 0.22 mm, respectively, and an extrusion multiplier of 0.96 (96%); (B) a layer height and width of 0.10 and 0.20 mm, respectively, and an extrusion multiplier of 1.0 (100%); and a layer height and width of (C) 0.08 and 0.18 mm, respectively, and an extrusion multiplier of 1.04 (104%).

It is possible to observe by the illustration in Fig. 9-I that the melted filament is extruded by the tip of the nozzle and solidifies in different shapes. Scanning electron microscopy images (SEM) of transversal views of the rasters in Fig. 9-II showed that the shapes could vary from rounded to oblong. For simplification, an oblong shape was considered ideal because of the greater filling of the voids and better sintering of the rasters and layers. Thus, Fig. 9A-I indicates that lower extrusion multiplier levels combined with higher layer height and raster width produce extruded lines with a rounded shape and weak bonding between them, followed by a lower contact area. Conversely, the conditions carried out in Fig. 9C promote the formation of oblong shapes of the extruded lines (Fig. 9C-II) and, consequently, a greater contact between the extruded and the adjacent raster. The results showed in Fig. 9C-III demonstrated more homogeneity due to the sintering, and a great printed device was achieved with few air gaps and voids. Accordingly, an

increase in the transparency of the printed devices was also observed, as depicted in Fig. 9C-IV.

The devices obtained under different conditions (Fig. 9A-C) can also be compared in a theoretical way according to eqn (2). Considering that the temperature  $T_r$  at a location  $x$ , the extrusion temperature  $T_{\text{extr}}$ , the temperature of the support  $T_{\text{sup}}$ , and the contact heat transfer coefficient  $h_{\text{supp}}$  between the filament and the support segment are the same under all conditions tested, the only variable to be considered is the fraction of the extruded line area in physical contact with another line,  $\lambda$ . Thus, greater values of  $\lambda$  are associated with few voids and an increase in the transparency of the layers. The terms  $K_1$  and  $K_2$  are related to heat transfer, and they influence mainly the resolution rather than the transparency.

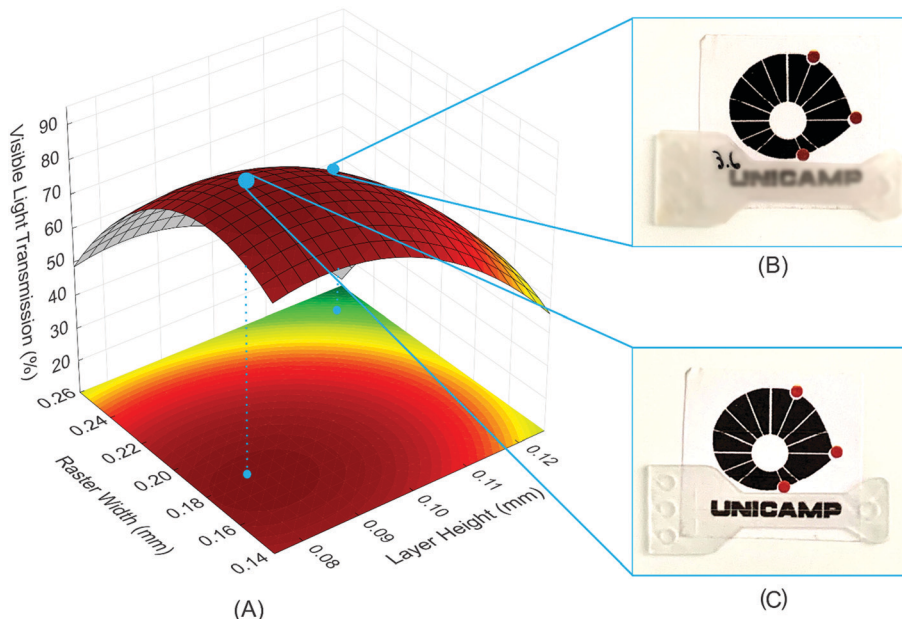
Therefore, to achieve transparency by optimizing the values of the main parameters of the 3D printer software, a random experimental planning was performed based on Box-Behnken using three variables: layer height, extrusion width, and multiplier extrusion with three levels each. The parameters and levels are presented in Table S4.<sup>†</sup>

Fig. 10A shows a response surface plot for visible light transmittance related to the height and width of the layer and two highlighted points with lower (Fig. 10B) and higher (Fig. 10C) transparency of the printed device. Based on these results, it was found that higher values of height and width of the layer lead to lower light transmission (%), as depicted in Fig. 10B, in which 28.5% transmittance was achieved. According to Romanov *et al.*, transparency can be reduced in this case because of the entrapment of microscopic air bubbles and light scattering from poorly bonded layers.<sup>26</sup> Conversely, greater light transmission was found for devices obtained with lower layer height and intermediate width values, as the device shown in Fig. 10C, which exhibited 82.2% light transmission. The greater transmittance values were associated with more uniformity of the layer deposition and the decrease in the number of voids and air gaps because of the higher proximity of the raster.

Moreover, a response surface contour plot of raster width vs. layer height was obtained (Fig. S13<sup>†</sup>) with the extrusion multiplier value kept at 104%. The results showed that a range of layer height and width values could be applied without loss in the transparency of the device. However, it is desired that the ratio between height and width follows eqn (3).

Finally, to obtain a microfluidic device with optimized transparency, an infill of 100% followed by an extrusion flow rate of 104% was used, while the extrusion temperature was kept at 230 °C, and the printing bed was maintained at 100 °C. The infill overlap was increased by 7% to eliminate air bubbles between the internal filling and the external wall of the device.

Fig. 11 shows the microfluidic device printed under optimized conditions. The device was printed within 17 min, presented 83.4% visible light transmission (640 μm thickness), and showed a channel width of 64.2 μm ± 7.9 μm. The standard deviation of the width was calculated using ten measurements in different regions of the channel.



**Fig. 10** (A) Response surface plot of the visible light transmittance with the height and the width of the extruded layer. (B) Transparency point (optical transmission 33.4%) with non-optimized parameters, where the layer height is 0.12 mm, and the layer width is 0.24 mm. (C) Transparency point (optical transmission 83.4%) with optimized parameters, in which the layer height and the raster width were 0.08 mm and 0.18 mm, respectively.

It is important to emphasize that most glasses show around 90% light transmission (Video S2†). Thus, the FDM-based manufacturing of devices with light transmission greater than 80% is a significant achievement, and it can satisfy a wide range of applications that were only feasible with devices printed using more expensive printing technologies. Table S5† shows the transmittances reported in other works for microfluidic devices printed using FDM, SLA, i3DP, and DLP techniques. The average transmittance value (80%) obtained in our work was significantly higher than those reported for FDM and comparable to those obtained using more complex and expensive printers.<sup>26,52–58</sup> Furthermore, the light transmission tests were performed with devices with a thickness of 640 µm (8 layers), while a microchannel was built with only two layers of distance (140 µm) from the base. It means that light transmission in the channel could be even better, allowing for instance coupling digital cameras to visualize reactions products, biological interactions, fluid phenomena, and other applications,

particularly analytical and bioanalytical assays with optical detection.

After optimizing the printing parameters, transparency improvements were also observed for the other thermoplastic materials studied. However, the obtained transmittance varied between 50 and 60% for those materials. Although these transmittance values can be considered high, mainly using FDM printers, they were much lower than those obtained for the devices printed using PETG.

Finally, a pressure test was performed to investigate the pressure resistance of the devices. The results showed that the microchannels could hold up to 80 bar (at around 1200 psi – the maximum pressure able to be applied by the syringe pump) without any leakage, failure, or channel deformation.

#### Robustness, precision, and reproducibility

One of the main promises of 3D-printed technology against soft-lithography techniques was to improve translating

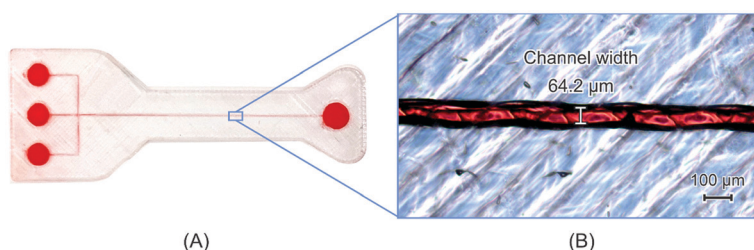


**Fig. 11** A microfluidic device fabricated using the FDM-based 3D printer under optimized conditions. (A) Whole view; (B) microchannel with 64.2 µm width.

microdevices to a commercial scale. However, it is not a new task that the microfabrication method needs to achieve great robustness, precision, and reproducibility for the fabrication and commercialization of microfluidic devices. Moreover, these merits are still challenging for 3D-printed technologies, especially FDM-based ones, due to some variables that will be addressed here.

First of all, the choice of the nozzle was found to be one of the main critical parameters for quality and resolution, followed by the software parameters to obtain transparent devices with microchannel size less than 100  $\mu\text{m}$ . However, for the efficacy and accuracy of these parameters, the frame structure and the printing bed material must also be considered. These components are related to the adhesion of the printed devices to the printing bed, unevenness of the frame structure, calibration problems, and vibrational effects, which can affect the roughness of the channel.

A small piece of quartz (7 cm  $\times$  5 cm and 3 mm thickness) was adapted and replaced the glass bed (commonly used in commercial FDM 3D printers) initially used (Fig. S11†). This adaptation was performed to improve the adhesion of the printed parts that is decreased on the glass printing bed because of the surface delamination caused by the typical application of adhesion promoters (such as polyvinylpyrrolidone-based glues) for PETG and ABS materials. This lower adhesion between the printed device and the printing bed can affect the repeatability of the printing process and cause deformation of the printed parts. Moreover, the use of a piece of quartz as a printing bed is attractive due to its lower coefficient of thermal expansion ( $0.5 \text{ m m}^{-1} \text{ K}^{-1}$ ) when compared to common glasses ( $9.0 \times 10^{-6} \text{ m m}^{-1} \text{ K}^{-1}$ ),<sup>59,60</sup> being able to receive thermal shocks up to 700 °C without suffering deformation. In addition, the high uniformity of the quartz surface and its good chemical resistance against the adhesion-promoting products make it an ideal material to use as a printing bed, particularly for building high-definition devices. However, as quartz has an effective high cost, only a small piece of this material was used but suitable to the size of the printed devices.

In addition to the choice of the printing bed material and all referred parameters, the mechanical vibrational effects are often neglected in the FDM printing processes, and they can directly affect printing definition and surface roughness. Although some post-printing methods can be applied to improve the smoothness of the 3D-printed surface, such as treatment with organic solvents, this interference can limit the resolution when micrometric internal structures are aimed. Moreover, the surface roughness can also affect the flow regime in a microchannel. Thus, vibrational tests were performed using a piezoelectric-based accelerometer to compare the mechanical vibration intensity of 3D printers using open and closed frame structures (cabinets).

As expected, the remarkable noisiest vibrational spectrum for the printer with an open cabinet (Fig. S12†) demonstrated a greater vibrational effect for this frame structure when compared to that for the closed cabinet (Fig. S12-II†). This

vibration can be attributed to the kinematic mechanism “three moving mechanism parallel machine tool” (usually known as 3-TPT mechanism), a parallel movement of the printing mechanisms in the coordinate plane X, Y, Z. For most of the FDM 3-D printers, the kinetic mechanism usually is different according to the cabinet frame structure. For the open cabinet printer, the movement in the y axis is responsible for more than 90% of the kinematic mechanism.<sup>61,62</sup> The torque applied by the Y printer motor of the open printer would be ideally unidirectional. However, it acts on all other axes of the twin-screw, the guide bars, pulleys, and other structures, giving rise to a resultant force acting perpendicular to the device on the printing bed.

On the other hand, the printing bed in a closed cabinet printer moves only in the z-axis (in the direction of layers), and it is responsible for 5% of the kinematic mechanism. The results showed a suitable printed device using the closed cabinet printer, presenting more uniform printed layers, few air gaps, and reduced channel deformation when compared with the device obtained in an open cabinet printer. Furthermore, a closed printer cabinet avoids air flows during the printing process, and consequently, it prevents printing deformation by sudden changes in temperature. Thus, using a closed cabinet printer is an interesting choice when micrometric structures are aimed.

In this way, under optimized conditions, devices printed in the same day ( $n = 10$ ) showed a precision of 10.8% (RSD) for an average channel width of 63.9  $\mu\text{m}$ . For devices printed in five different days, a value of 16.1% (RSD) was achieved for an average channel width of 66.9  $\mu\text{m}$ . In terms of transparency,  $79.7\% \pm 6.8$  light transmission was observed for all devices tested. Thus, the results achieved are expressive and demonstrated reproducibility of the channels and suitable transparency values for FDM 3D printing of microdevices.

### Requirement for drawing design adjustments

Besides nozzle adaptation, vibrational control, and optimization on software parameters, the design of the device must be considered to produce FDM-based 3D-printed microfluidic devices containing channels with dimensions of less than 100  $\mu\text{m}$ . The main reason associated with that is the major exposure of micrometric areas of the draw to the heat flow. Some intersections of the microchannel can be completely blocked when narrow geometries are designed without considering the XY movement of the nozzle (during filament deposition) and the exposure time of heated areas of the extrusion system (considering the low printing speed).

To address the phenomena, Fig. 12 depicts (A) printed channels with a typical drawing, (B) simulation of the heating distribution due to the extrusion process, and (C) a drawing with adjustments in microchannel design. It is possible to observe that the top region of the draw remains exposed to heat flow for a longer time, and it is characterized as a critical region in Fig. 12B, especially because the heated

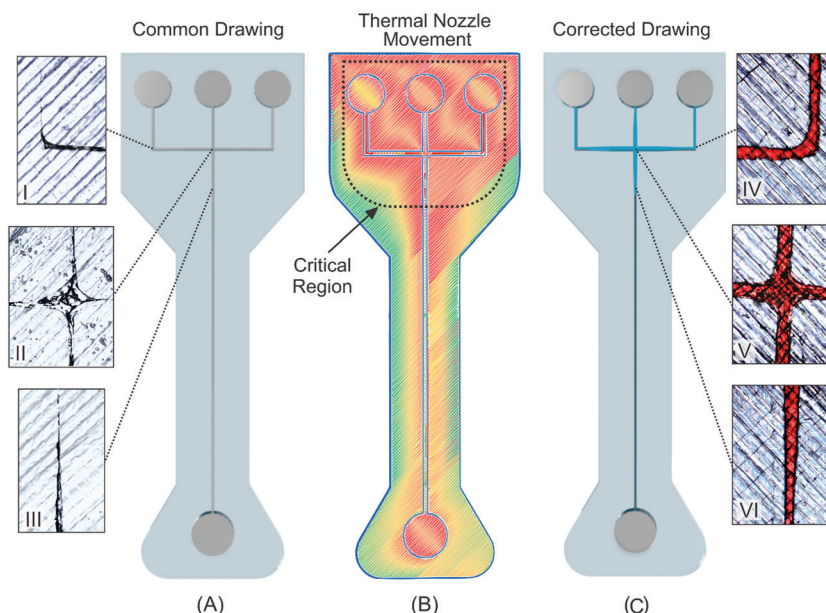


**Fig. 12** (I)–(III) Intersections blocked due to greater channel exposure to the heated nozzle. (A) Design of the device with narrow geometries; (B) simulation of the heated system movement in the deposition of the raster during the printing; (C) corrected design, considering an enlargement of 10% of more critical regions; (IV), (V) and (VI) intersections without obstructions printed using the layout with corrections.

nozzle remains in this specific region for longer times. These effects are in close agreement with the results discussed earlier regarding undesired heating effects.

Thus, the microchannel designed in Fig. 12A showed printing problems, such as partial or complete clogging of the microchannels. These problems are common challenges in manufacturing microfluidic devices using FDM printing, particularly when performed at a low printing speed. However, an adjustment in the drawing design was found to overcome these problems. As shown in Fig. 12C, the microchannels were projected to be 10% larger than the expected channel width, only in the critical region of the device. Using this correction, the clogging of the microchannel intersection was prevented in the printed microdevice.

Unfortunately, there is no general rule or linear correction to obtain the right parameter values that can be applied for any microdevice design. In this way, it is interesting to optimize the layout to predict regions with greater heat incidence and compensate for this excessive heating effect. Thus, different designs can be achieved, and complex microfluidic devices can be printed without loss of resolution in the microchannels produced by FDM-based technology. Fig. S14† shows printed devices with other designs that were successfully adjusted.

## Conclusions

We demonstrated using theoretical and experimental methods that FDM-based 3D-printing has great potential to fabricate microfluidic devices with good robustness, precision, reproducibility, and higher resolution and

transparency (for visible light) than those already reported in the literature. This remarkable improvement of FDM 3D printing was achieved by understanding and optimizing several parameters and printing characteristics. Additionally, the geometry of the nozzle was demonstrated to be another critical parameter because only the adapted nozzle allowed channels with widths lower than 100  $\mu\text{m}$  to be printed. We also found that this microchannel could support more than 80 bar of pressure without leakage.

Accordingly, when microchannels are aimed, it is also important to attend to some details, such as vibrational effects and the materials of the printing bed. These parameters are commonly neglected, mainly because their adverse effects are not pronounced on a macroscopic scale. Nevertheless, it was proved that using FDM printers to obtain channels with widths lower than 100  $\mu\text{m}$ , good transparency, and layer uniformity, the control and calibration of these effects are necessary.

The optimizations described in this work can make FDM 3D printing suitable to produce microdevices that require structures with sizes smaller than 100  $\mu\text{m}$ , for instance in microchannels to perform capillary electrophoresis separations. The transparency (80% light transmittance) of the 3D-printed devices was comparable to that observed for most glasses, and it was above that reported for devices printed in 3D SLA printers. This glass-like transparency in microfluidic devices is an impressive achievement for optical detection of colored compounds or microscopic visualization of physical-chemical processes, such as formation and aggregation of particles, drop generation and coalescence, solution color change, mixture efficiency, and several other applications.

It is important to emphasize that there is no “ideal recipe” when building a device by FDM 3D printing. However, considering the expected effects discussed here in the design process, the full potential of FDM technology can be attained.

Finally, we believe that this work can contribute to a better understanding of the FDM 3D printing process and opens up new possibilities for using this technique to fabricate microfluidic and transparent devices for several applications, particularly for analytical and bioanalytical assays.

## Conflicts of interest

The authors declare no competing financial interest.

## Acknowledgements

The authors acknowledge the financial support provided by Fundação de Amparo à Pesquisa do Estado de São Paulo (FAPESP grants #2013/22127-2, #2018/13496-8, 2018/06478-3), National Council for Scientific and Technological Development (CNPq grant #140545/2017/4, #305447/2019-0), Instituto Nacional de Ciência e Tecnologia em Bioanalítica (INCTBio grant #2014/50867-3 FAPESP) and Coordenação de Aperfeiçoamento de Pessoal do Ensino Superior (CAPES, #88887.372944/2019-00 – Finance code 001).

## References

- 1 S. Haeberle and R. Zengerle, *Lab Chip*, 2007, **7**, 1094–1110.
- 2 V. Faustino, S. O. Catarino, R. Lima and G. Minas, *J. Biomech.*, 2016, **49**, 2280–2292.
- 3 S. Dagher, A. Hilal-Alnaqbi, B. Akhozheya, L. Akhu-Zaheya and A. Dhabi, *Biointerface Res. Appl. Chem.*, 2021, **11**, 11996–12005.
- 4 C. Iliescu, H. Taylor, M. Avram, J. Miao and S. Franssila, *Biomicrofluidics*, 2012, **6**, 16505.
- 5 L. Y. Yeo, H. C. Chang, P. P. Y. Chan and J. R. Friend, *Small*, 2011, **7**, 12–48.
- 6 D. C. Duffy, J. C. McDonald, O. J. A. Schueller and G. M. Whitesides, *Anal. Chem.*, 1998, **70**, 4974–4984.
- 7 N. Bhattacharjee, A. Urrios, S. Kang and A. Folch, *Lab Chip*, 2016, **16**, 1720–1742.
- 8 S. Waheed, J. M. Cabot, N. P. Macdonald, T. Lewis, R. M. Guijt, B. Paull and M. C. Breadmore, *Lab Chip*, 2016, **16**, 1993–2013.
- 9 A. K. Au, W. Huynh, L. F. Horowitz and A. Folch, *Angew. Chem., Int. Ed.*, 2016, **55**, 3862–3881.
- 10 T. C. Lee, R. Ramlan, N. Shahrubudin, T. C. Lee and R. Ramlan, *Procedia Manuf.*, 2019, **35**, 1286–1296.
- 11 A. V. Nielsen, M. J. Beauchamp, G. P. Nordin and A. T. Woolley, *Annu. Rev. Anal. Chem.*, 2020, **13**, 45–65.
- 12 C. Chen, B. T. Mehl, A. S. Munshi, A. D. Townsend, D. M. Spence and R. S. Martin, *Anal. Methods*, 2016, **8**, 6005–6012.
- 13 V. Mehta and S. N. Rath, *Bio-Des. Manuf.*, 2021, **4**, 311–343.
- 14 C. M. B. Ho, S. H. Ng, K. H. H. Li and Y. J. Yoon, *Lab Chip*, 2015, **15**, 3627–3637.
- 15 N. Bhattacharjee, A. Urrios, S. Kang and A. Folch, *Lab Chip*, 2016, **16**, 1720–1742.
- 16 E. K. Sackmann, A. L. Fulton and D. J. Beebe, *Nature*, 2014, **507**, 181–189.
- 17 S. N. Bhatia and D. E. Ingber, *Nat. Biotechnol.*, 2014, **32**, 760–772.
- 18 R. F. Quero, L. P. Bressan, J. A. F. da Silva and D. P. de Jesus, *Sens. Actuators, B*, 2019, **286**, 301–305.
- 19 L. P. Bressan, J. Robles-Najar, C. B. Adamo, R. F. Quero, B. M. C. Costa, D. P. de Jesus and J. A. F. da Silva, *Microchem. J.*, 2019, **146**, 1083–1089.
- 20 L. P. Bressan, C. B. Adamo, R. F. Quero, D. P. De Jesus and J. A. F. Da Silva, *Anal. Methods*, 2019, **11**, 1014–1020.
- 21 L. P. Bressan, T. M. Lima, G. D. da Silveira and J. A. F. da Silva, *SN Appl. Sci.*, 2020, **11**, 11996–12005.
- 22 N. P. Macdonald, J. M. Cabot, P. Smejkal, R. M. Guijt, B. Paull and M. C. Breadmore, *Anal. Chem.*, 2017, **89**, 3858–3866.
- 23 H. H. Hwang, W. Zhu, G. Victorine, N. Lawrence and S. Chen, *Small Methods*, 2018, **2**, 1–18.
- 24 H. K. Balakrishnan, F. Badar, E. H. Doeven, J. I. Novak, A. Merenda, L. F. Dumée, J. Loy and R. M. Guijt, *Anal. Chem.*, 2021, **93**, 350–366.
- 25 M. D. Nelson, N. Ramkumar and B. K. Gale, in *23rd International Conference on Miniaturized Systems for Chemistry and Life Sciences, MicroTAS 2019*, IOP Publishing, 2019, pp. 1108–1109.
- 26 V. Romanov, R. Samuel, M. Chaharlang, A. R. Jafek, A. Frost and B. K. Gale, *Anal. Chem.*, 2018, **90**, 10450–10456.
- 27 N. A. Sukindar, M. K. A. Ariffin, B. T. Hang Tuah Baharudin, C. N. A. Jaafar and M. I. S. Ismail, *J. Teknol.*, 2016, **78**, 7–15.
- 28 N. Mostafa, H. M. Syed, S. Igor and G. Andrew, *Tsinghua Sci. Technol.*, 2009, **14**, 29–37.
- 29 A. Bellini, S. Gücü and M. Bertoldi, *J. Manuf. Sci. Eng.*, 2004, **126**, 237–246.
- 30 J. Z. Liang and J. N. Ness, *Polym. Test.*, 1997, **16**, 403–412.
- 31 M. Lalegani Dezaki, M. K. A. Mohd Ariffin and S. Hatami, *Rapid Prototyp. J.*, 2021, **3**, 562–582.
- 32 F. Cverna, *Thermal Properties of Metals*, ASM International, 2002.
- 33 H. Brooks, A. Rennie, T. Abram, J. McGovern and F. Caron, Variable fused deposition modelling - concept design and tool path generation, *12th Rapid Des. Prototyp. Manuf. Conf.*, Lancaster, 2011, pp. 113–122.
- 34 T. Y. Emre Koc and O. Gunel, in *International conference on energy and thermal engineering: Istanbul*, 2017, pp. 25–28.
- 35 A. Dey and N. Yodo, *J. Manuf. Mater. Process.*, 2019, **3**, 64.
- 36 O. A. Mohamed, S. H. Masood and J. L. Bhowmik, *Adv. Manuf.*, 2015, **3**, 42–53.
- 37 C. Bellehumeur, L. Li, Q. Sun and P. Gu, *J. Manuf. Process.*, 2004, **6**, 170–178.
- 38 W. Tang, H. Liu, L. Zhu, J. Shi, Z. Li, J. Xiang and J. Yang, *Micromachines*, 2019, **10**, 554.
- 39 T. Nanchariah, D. R. Raju and V. R. Raju, *Int. J. Emerging Technol.*, 2010, **1**, 106–112.
- 40 F. Pigeonneau, D. Xu, M. Vincent and J. F. Agassant, *Addit. Manuf.*, 2020, **32**, 10101.

- 41 P. Geng, J. Zhao, W. Wu, W. Ye, Y. Wang, S. Wang and S. Zhang, *J. Manuf. Process.*, 2019, **37**, 266–273.
- 42 J. Wang, H. Xie, Z. Weng, T. Senthil and L. Wu, *Mater. Des.*, 2016, **105**, 152–159.
- 43 F. Bähr and E. Westkämper, in *Procedia CIRP*, Elsevier B.V., 2018, vol. 72, pp. 1214–1219.
- 44 O. Pokluda, C. T. Bellehumeur and J. Vlachopoulos, *AIChE J.*, 1997, **43**, 3253–3256.
- 45 S. F. Costa, F. M. Duarte and J. A. Covas, *Virtual Phys. Prototyp.*, 2015, **10**, 35–46.
- 46 S. F. Costa, F. M. Duarte and J. A. Covas, *J. Mater. Process. Technol.*, 2017, **245**, 167–179.
- 47 S. Garzon-Hernandez, D. Garcia-Gonzalez, A. Jérusalem and A. Arias, *Mater. Des.*, 2020, **188**, 108414.
- 48 D. Bhalodi, K. Zalavadiya and P. K. Gurrala, *J. Braz. Soc. Mech. Sci. Eng.*, 2019, **41**, 1–11.
- 49 P. K. Penumakala, J. Santo and A. Thomas, *Composites, Part B*, 2020, **201**, 108336.
- 50 P. Wolszczak, K. Lygas, M. Paszko and R. A. Wach, *Rapid Prototyp. J.*, 2018, **24**, 615–622.
- 51 M. A. A. Rehmani, S. A. Jaywant and K. M. Arif, *Micromachines*, 2021, **12**, 1–20.
- 52 F. Kotz, M. Mader, N. Dellen, P. Risch, A. Kick, D. Helmer and B. E. Rapp, *Micromachines*, 2020, **11**, 873.
- 53 A. M. Tothill, M. Partridge, S. W. James and R. P. Tatam, *J. Micromech. Microeng.*, 2017, **27**, 035018.
- 54 P. Petrov, D. Agzamova, V. Pustovalov, E. Zhikhareva, B. Saprykin, I. Chmutin and N. Shmakova, *Micromachines*, 2020, **11**, 873.
- 55 H. He, M. Gao, B. Illés and K. Molnar, *Int. J. Bioprint.*, 2020, **6**, 2134–2141.
- 56 A. I. Shallan, P. Smejkal, M. Corban, R. M. Guijt and M. C. Breadmore, *Anal. Chem.*, 2014, **86**, 3124–3130.
- 57 A. P. Kuo, N. Bhattacharjee, Y.-S. Lee, K. Castro, Y. T. Kim and A. Folch, *Adv. Mater. Technol.*, 2019, **4**, 1800395.
- 58 R. Walczak, K. Adamski and W. Kubicki, *Sens. Actuators, B*, 2018, **261**, 474–480.
- 59 J. J. Tully and G. N. Meloni, *Anal. Chem.*, 2020, **92**, 14853–14860.
- 60 B. Dralle, G. Kitaigorodskij, S. C. Schulz and S. T. Ullmann, in *Silicates*, Elsevier, 1968, vol. 2, pp. 292–407.
- 61 A. Srivastava, C. Gautam, N. Bhan and R. Dayal, *IOP Conf. Ser.: Mater. Sci. Eng.*, 2019, **594**, 012020.
- 62 C. Zhu and Z. Zhao, *Mech. Sci.*, 2019, **10**, 287–298.